ACS Catalysis

pubs.acs.org/acscatalysis
Research Article

CO_2 Hydrogenation to Methanol Catalyzed by Mn-SNS Complex: Role of *fac*/*mer* Isomerism on Catalytic Reactivities

Sai V. C. Vummaleti,[§] Huiwen Tan,[§] Jingyi Liu, and Xinglong Zhang*

Cite This: https://doi.org/10.1021/acscatal.6c03391
Read Online

ABSTRACT: We present a DFT investigation of the indirect hydrogenation of CO_2 to methanol catalyzed by a Mn–SNS complex (**Mn-*fac***) in the presence of morpholine as a co-catalyst. Formation of the active hydride species [MnH–NH] (**1**) proceeds with a kinetic preference for **1-*mer***, while interconversion enables access to **1-*fac*** under the reaction conditions. Mechanistic analysis reveals complementary roles of the two hydride species, with **1-*fac*** promoting CO_2 hydrogenation to formic acid and **1-*mer*** facilitating the subsequent reduction of *N*-formylmorpholine to methanol via a kinetically favorable pathway involving C–N bond hydrogenation followed by C═O bond hydrogenation. This pathway exhibits a lower energetic span for **1-*mer*** (δE = 35.0 (32.3) kcal/mol) than for **1-*fac*** (δE = 42.3 (38.6) kcal/mol). The overall reactivity is primarily governed by heterolytic H_2 activation and is strongly influenced by the ligand *trans* to H_2, where increasing π-acceptor character destabilizes the H_2-coordinated intermediates and leads to higher activation barriers. These findings establish the cooperative roles of **1-*fac***/**1-*mer*** hydride species and underscore the importance of the *trans* ligand in governing the catalytic performance in Mn–SNS systems for CO_2 hydrogenation.

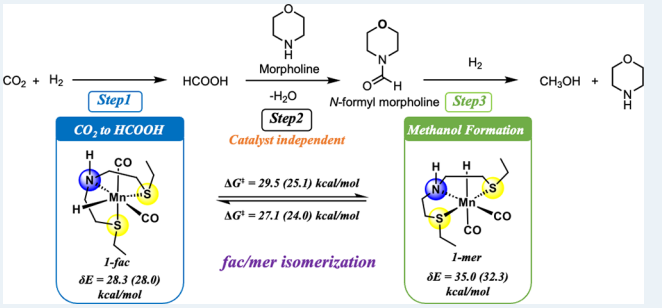

KEYWORDS: *Mn catalyst, CO_2 hydrogenation, fac/mer conversion, density functional theory calculations, methanol*

INTRODUCTION

The increasing global energy demand, driven by population growth, has led to a substantial rise in CO_2 emissions, primarily associated with fossil fuel consumption. Consequently, strategies that transform CO_2 through capture and catalytic hydrogenation, commonly referred to as carbon capture, utilization, and storage (CCUS), have emerged as promising approaches to address both energy and climate challenges.[1−5] One promising strategy involves the chemical conversion of CO_2 into value-added products such as methanol, formic acid, and formaldehyde.[6−12] Among these, methanol is particularly attractive due to its potential as an alternative fuel and an important industrial feedstock. Traditionally, methanol synthesis relies on fossil-derived syngas, whereas the direct hydrogenation of CO_2 offers a more sustainable alternative.[13−16] Industrially, methanol is produced from synthesis gas (CO, H_2, and CO_2) over Cu/ZnO/Al_2O_3-based heterogeneous catalysts under elevated temperature and pressure conditions, and similar catalytic systems have also been applied for CO_2 hydrogenation.[17−20] Despite their effectiveness, these heterogeneous catalysts typically operate under harsh conditions, including elevated temperatures and pressures, which can limit their overall efficiency.[21] This has led to increasing interest in homogeneous catalysts, which enable CO_2 hydrogenation under milder conditions with improved control over reactivity and selectivity.

Notable early contributions in the field came from the Leitner[22] and Sanford[23] groups, who demonstrated Ru-based systems for CO_2 hydrogenation to methanol. The Leitner group employed Ru-phosphine catalysts for direct CO_2 hydrogenation (Scheme 1A), whereas the Sanford group utilized PNN pincer complexes in a cascade catalytic approach to access methanol. Over the past decade, homogeneous catalysts incorporating noble metals such as Ru and Ir have been extensively studied for direct[24−26] and indirect[27−29] CO_2 reduction to CH_3OH under relatively mild reaction conditions. Among these advancements, a promising strategy reported by the Sanford group employed a Ru catalyst with a PNP ligand and dimethylamine ($NHMe_2$) as a co-catalyst.[25] This system achieved efficient CO_2 capture through carbamate salt formation, followed by hydrogenation to methanol, attaining >95% CO_2 conversion (Scheme 1B). The incorporation of amines in this process offers a potential route to integrate CO_2 hydrogenation

Received: April 29, 2026
Revised: July 30, 2026
Accepted: July 31, 2026

https://doi.org/10.1021/acscatal.6c03391
ACS Catal. XXXX, XXX, XXX−XXX

Scheme 1. Homogeneous Transition Metal Catalysts for CO_2 Hydrogenation to Methanol: (A) Ru–Phosphine-Catalyzed Direct Hydrogenation; (B) Tandem Amine-Capture/Ru-Catalyzed Hydrogenation; (C) Co/Triphos-Catalyzed Hydrogenation; (D) Mn–PNP-Catalyzed Indirect Hydrogenation via an *N*-Formylamine Intermediate; and (E) Mn–SNS-Catalyzed Indirect Hydrogenation via *N*-Formylmorpholine

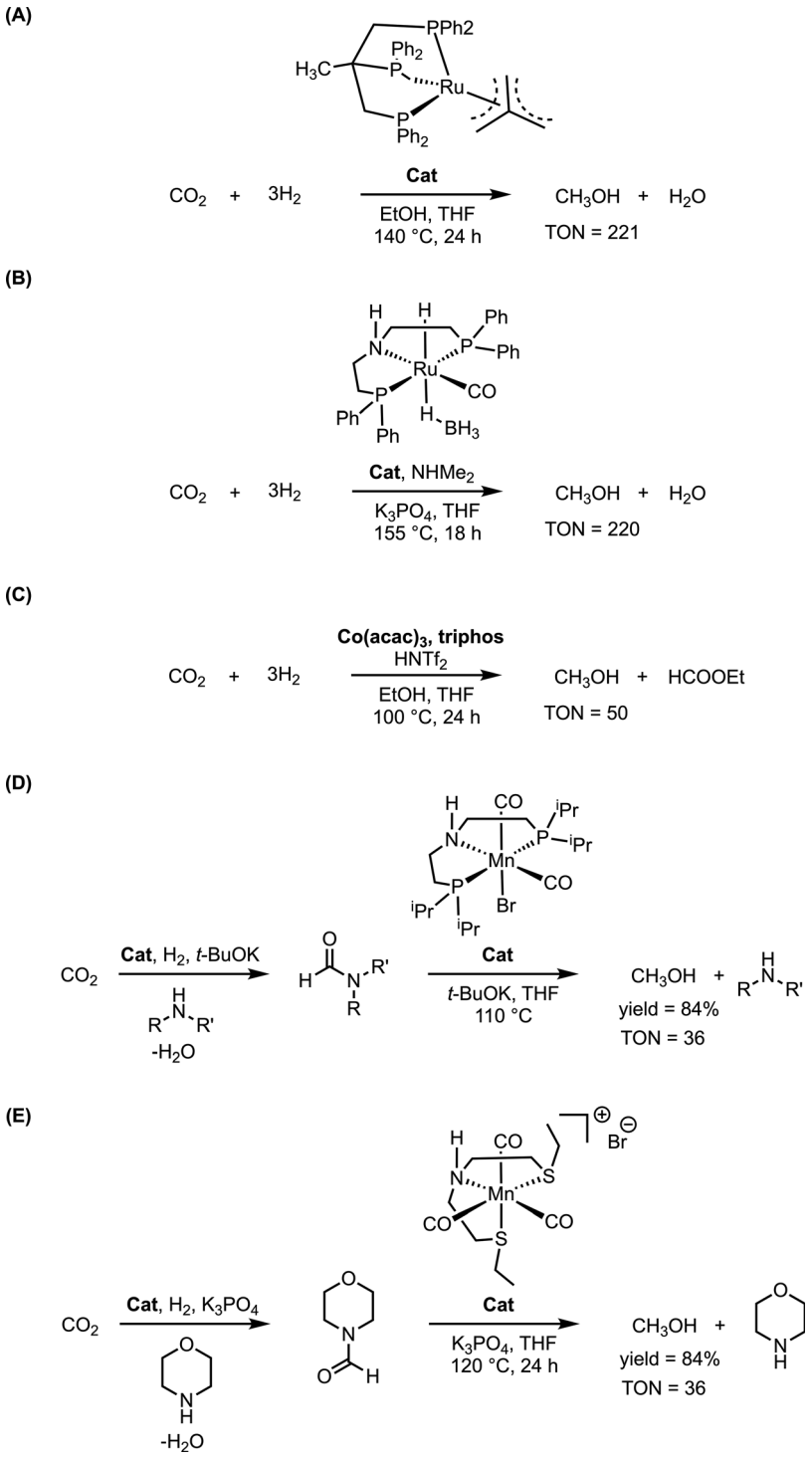

with carbon capture technologies. However, the reliance on expensive noble metals and ligands, combined with relatively low turnover numbers (TONs), limits the feasibility of these systems for large-scale methanol production.

In recent years, efforts have focused on developing cost-effective, earth-abundant non-noble metal catalysts, such as Co, Mn, and Fe, for CO_2 hydrogenation to methanol. The Beller group reported an *in situ*-generated Co-based catalyst with a Triphos ligand achieving a TON of up to 78 for methanol formation (Scheme 1C).[30] Prakash and co-workers reported a Mn catalyst with a PNP pincer ligand for indirect CO_2 hydrogenation using morpholine as a co-catalyst,

https://doi.org/10.1021/acscatal.6c03391
ACS Catal. XXXX, XXX, XXX–XXX

achieving 95% conversion of morpholine to *N*-formylmorpholine and a maximum TON of 128 for methanol formation (Scheme 1D).[31] Inspired by these studies, Mandal et al. performed detailed DFT and microkinetic studies to elucidate the mechanism of CO_2 hydrogenation to methanol catalyzed by Mn(I), Fe(II), and Ru(II) PNP complexes.[32] For these systems, they proposed a pathway involving CO_2 hydrogenation to formic acid, its amidation to *N*-formylmorpholine, and subsequent hydrogenation to methanol, with heterolytic H_2 cleavage identified as the turnover-limiting step (38.2 kcal/mol). Their computed mechanism was consistent with the available experimental observations and provided an important mechanistic framework for amine-assisted CO_2 hydrogenation. The Mn-PNP catalyst system that was studied adopts only the *mer* form, where the P, N, P atoms all lie on the same plane. The *fac* form of the Mn-PNP system may not be sterically favorable, as this arrangement would put two bulky P atoms adjacent to each other in the coordination sphere of the Mn metal center. These findings established for PNP-supported metal complexes may not be directly applicable to other ligand environments. In particular, changes in ligand donor set, coordination geometry, and metal–ligand cooperativity may substantially alter the nature of the active species, the H_2 activation barrier, and the preferred hydrogenation sequence. Catalyst-specific DFT studies remain necessary to understand how different ligand frameworks govern reactivity and selectivity in CO_2-to-methanol catalysis.

Very recently, Grover et al. reported a Mn–SNS catalyst[33] for the indirect hydrogenation of CO_2 to methanol, where morpholine served as a CO_2 capturing agent, achieving a 91% yield of *N*-formylmorpholine, which was subsequently hydrogenated to methanol under optimized conditions (120 °C, 10 atm H_2, 24 h, THF as solvent, and K_3PO_4 as base) (Scheme 1E). This catalytic system is of particular interest due to the earth-abundant nontoxic Mn center and the readily synthesizable SNS ligand, making it an ideal candidate for the mechanistic investigation of CO_2 hydrogenation to methanol. Unlike the previously studied Mn–PNP platform, this system features a distinct SNS ligand environment that can access different coordination modes at the Mn center, both of which can have a major influence on catalyst activation and the key H_2 cleavage step. These differences make the Mn–SNS system an important and nontrivial target for mechanistic investigation. In the present study, we investigate the reaction mechanism of CO_2 hydrogenation to methanol catalyzed by the Mn–SNS complex containing the SNS ligand in a facial (*fac*) coordination mode (**Mn-*fac***), using DFT calculations, building on the recent work by Mandal et al. on the Mn–PNP complex.[32]

We begin by examining the formation of the catalytically active manganese hydride species [HMn–NH] (**1**) from the **Mn-*fac*** precatalyst, considering both facial (*fac*) and meridional (*mer*) coordination modes (**1-*fac*** and **1-*mer***), followed by a detailed investigation of the CO_2 to methanol mechanism. The overall transformation proceeds through three key steps: (i) hydrogenation of CO_2 to formic acid catalyzed by complex **1**; (ii) formylation of morpholine to form *N*-formylmorpholine (a catalyst-independent step); and (iii) reduction of *N*-formylmorpholine to methanol by complex **1** (Scheme 1E). For the final step, we explored two alternative pathways: (a) C═O bond hydrogenation followed by C–N bond hydrogenation and (b) C–N bond hydrogenation followed by C═O bond hydrogenation. This study elucidates how the coordination mode of the SNS ligand at the Mn center governs key activation barriers and thereby dictates pathway selectivity in the conversion of *N*-formylmorpholine to methanol. Overall, these DFT results provide valuable insights into the catalytic conversion of CO_2 to methanol by manganese hydride complex **1**, highlighting the influence of the ligand *trans* to H_2 on the crucial heterolytic H_2 cleavage barrier.

■ COMPUTATIONAL DETAILS

Density functional theory (DFT) calculations were performed with *Gaussian 16* rev. B.01.[34] Geometry optimizations were initially performed using the B3LYP functional[35,36] with a mixed Karlsruhe-family basis set of triple-ζ valence def2-TZVPPD (where "D" indicates diffuse basis functions) for Mn[37,38] atom and def2-SVP[39,40] for all other atoms. Grimme's DFT-D3 dispersion correction with Becke–Johnson damping[41,42] (hereafter denoted B3LYP-D3BJ) has been included in all our calculations to account for the noncovalent interactions. Minima and transition structures on the potential energy surface (PES) were confirmed using harmonic frequency analysis at the same level of theory, showing respectively zero and one imaginary frequency. To assess the effect of geometry optimization in the gas phase vs in implicit solvation phase, we optimized key TSs (**TS_*fac*** and **TS_*mer***) in implicit solvation and found that the structures remain similar, with an RMSD of 0.014 to 0.027 Å (Supporting Information Section S7).

Single point (SP) corrections were performed using separately B3LYP-D3BJ and MN15 functional[43] with def2-QZVP[39] basis set for all atoms. The SMD implicit continuum solvation model[44] was used to account for the effect of tetrahydrofuran (THF) solvent on the computed Gibbs energy profile. Gibbs energies were evaluated at the reaction temperature of 393.15 K (120 °C), using a quasi-RRHO treatment of vibrational entropies.[45] Vibrational entropies of frequencies below 100 cm^{-1} were obtained according to a free rotor description, using a smooth damping function to interpolate between the two limiting descriptions. The free energies were further corrected using a standard concentration of 1 mol/L, which were used in solvation calculations. The final SMD(THF)-B3LYP-D3BJ/def2-QZVP//B3LYP-D3BJ/BS1 Gibbs energies, with SMD(THF)-MN15/def2-QZVP//B3LYP-D3BJ/BS1 values included in parentheses, are used for discussion throughout. *All Gibbs energy values in the text and figures are quoted in kcal/mol.* All molecular structures and molecular orbitals were visualized using *PyMOL* software.[46] Job submissions and all results analysis including thermochemistry (no natural abundance weighting) and electronic structures were performed using *CHEMSMART* automation toolkit.[47]

■ RESULTS AND DISCUSSION

Formation of Catalytically Active Manganese Hydride Species, 1-*fac* and 1-*mer*

The crystal structure of the Mn–SNS complex shows a facial (*fac*) coordination of the SNS ligand at the Mn center (**Mn-*fac***). DFT calculations indicate that the alternative *mer* isomer (**Mn-*mer***) lies 2.2 (1.4) kcal/mol higher in free energy (Figure S1 in the Supporting Information), therefore, **Mn-*fac*** is adopted as the reference precatalyst. Starting from **Mn-*fac***,

https://doi.org/10.1021/acscatal.6c03391
ACS Catal. XXXX, XXX, XXX–XXX

we examined the formation of the active hydride [HMn–NH] complex (**1**) in both *fac* and *mer* coordination modes, given that PNP- and SNS-based pincer ligands are known to undergo *fac*/*mer* interconversion under catalytic conditions,[48−50] thereby affording the corresponding **1-*fac*** and **1-*mer*** isomers, Figure 1. As the initial step, we investigated the dissociation of two possible CO ligands from **Mn-*fac***, located either *cis* or *trans* to the N atom. Our results indicate that the dissociation of CO *cis* to N is thermodynamically favorable, forming complex **A-*fac*** (9.4 (5.8) kcal/mol above **Mn-*fac***), which is 3.5 (3.6) kcal/mol more stable than complex **B-*fac*** (12.9 (9.4) kcal/mol above **Mn-*fac***), where CO *trans* to the N atom is dissociated. Structurally, both complex **A-*fac*** and complex **B-*fac*** feature coordination of the counter anion (Br^-) at the vacant site created by the respective CO dissociation, Figure 1.

Next, the removal of bromine as KBr, along with the formation of K_2HPO_4 in the presence of K_3PO_4, results in the penta-coordinated Mn complex, complex **C-*fac***. This step is endergonic, with complex **C-*fac*** lying 24.8 (23.2) kcal/mol above **Mn-*fac***, Figure 1. From **C-*fac***, heterolytic cleavage of H_2 at the vacant site, accompanied by the transfer of the hydridic and protonic hydrogens to the Mn and N atoms, respectively, yields the catalyst species **1-*fac***, Figure 1. This step is exergonic, with **1-*fac*** lying 15.6 (20.4) kcal/mol below **C-*fac*** and proceeds via **TS_*fac*** (Figure 2a), which has an activation free energy barrier of 13.9 (4.8) kcal/mol (corresponding to an overall barrier of 38.7 (27.9) kcal/mol from **Mn-*fac***), Figure 1. Alternatively, from **C-*fac***, rotation along the C–N bond via **TS_*iso*** facilitates *fac*-to-*mer* isomerization of the SNS ligand at the Mn center, with a low activation barrier of 2.3 (2.4) kcal/mol, yielding the more stable complex **C-*mer***, lying 18.4 (19.0) kcal/mol below **C-*fac***, Figure 1. The enhanced stability of **C-*mer*** can be attributed to its trigonal-bipyramidal geometry, which is less sterically crowded than the square-pyramidal arrangement observed for **C-*fac***. Subsequent heterolytic cleavage of H_2 at the vacant site of **C-*mer*** via **TS_*mer*** (Figure 2b), with an activation barrier of 27.4 (18.5) kcal/mol, yields the alternative catalyst species **1-*mer***, Figure 1. Notably, the facile *fac*-to-*mer* rearrangement of the SNS ligand via **TS_*iso*** is particularly significant as the overall barrier for the formation of **1-*mer*** (33.8 (22.7) kcal/mol from **Mn-*fac***) is 4.9 (5.2) kcal/mol lower than that for **1-*fac*** (38.7 (27.9) kcal/mol from **Mn-*fac***), indicating that **1-*mer*** is the kinetically preferred hydride species.

Considering that K_3PO_4 was used experimentally as the base and that countercation effects have been reported for related Mn(I) hydride catalysts,[51] we further examined the role of the potassium countercation. In the newly optimized

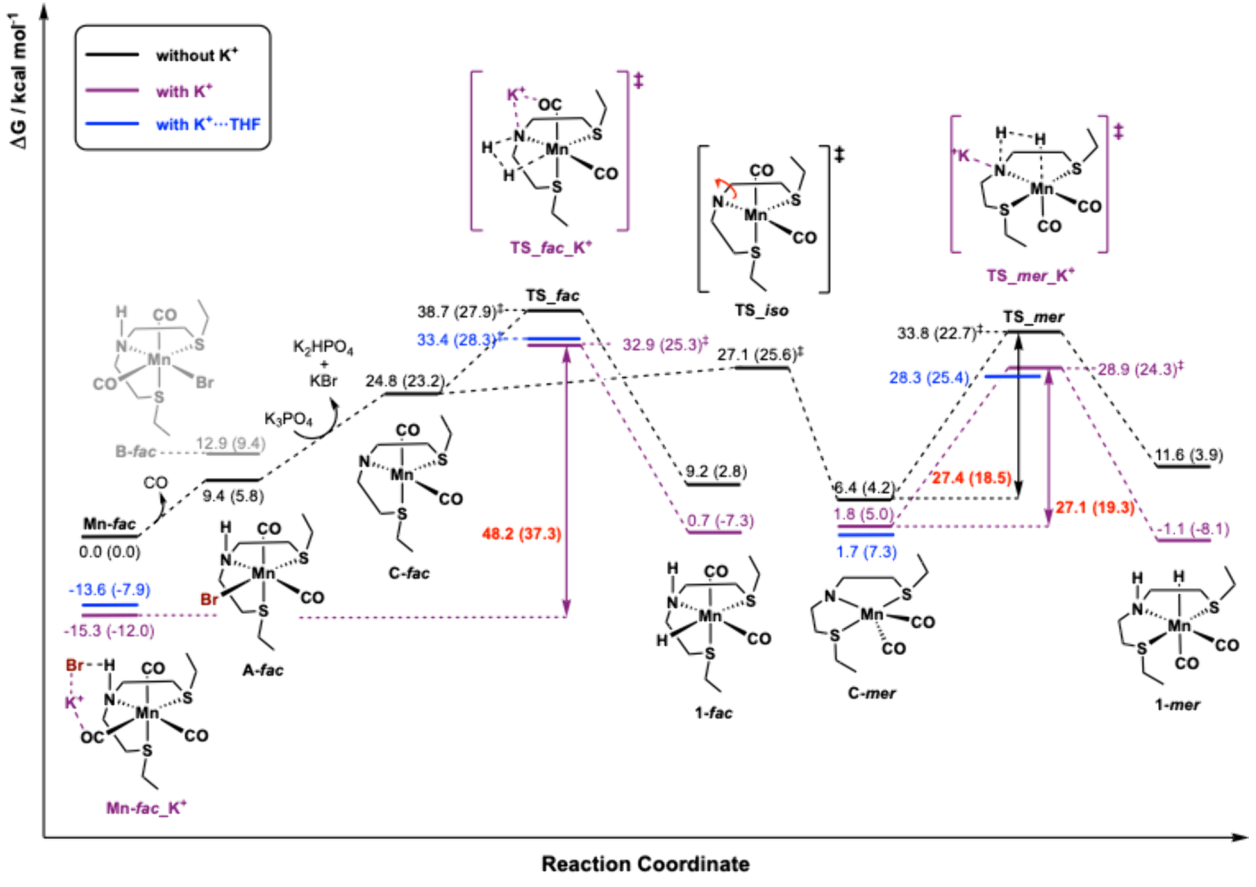

Figure 1. Reaction network for the formation of the active hydride [HMn–NH] complexes (**1-*fac*** and **1-*mer***) from the Mn–SNS precatalyst (**Mn-*fac***), in the presence and absence of K^+ countercation. The free energies were computed at SMD(THF)-B3LYP-D3BJ/def2-QZVP//B3LYP-D3BJ/(def2-TZVPPD for Mn and Br, while def2-SVP for all other atoms) level of theory. Corresponding free energies computed at the SMD(THF)-MN15/def2-QZVP//B3LYP-D3BJ/(def2-TZVPPD for Mn and Br, def2-SVP for all other atoms) level are given in parentheses. All energies are given in kcal/mol with respect to **Mn-*fac***.

https://doi.org/10.1021/acscatal.6c03391
ACS Catal. XXXX, XXX, XXX–XXX

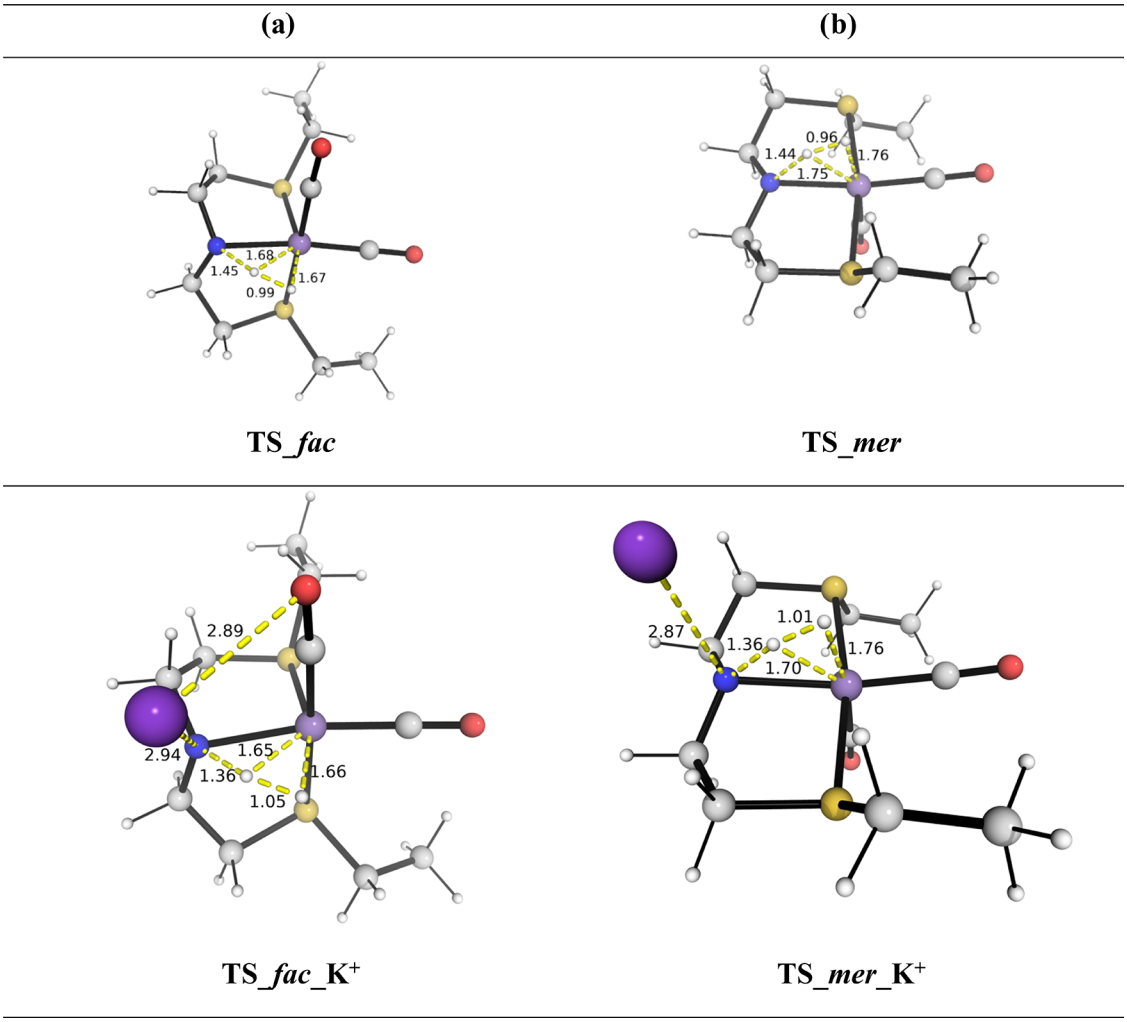

Figure 2. Crucial TS structures for heterolytic H_2 cleavage during the activation of the **Mn-*fac*** precatalyst to the active hydride [MnH–NH] (**1**) in the absence and the presence of K^+ countercation: (a) **TS_*fac*** and **TS_*fac*_K$^+$** for **1-*fac*** formation and (b) **TS_*mer*** and **TS_*mer*_K$^+$** for **1-*mer*** formation. Selected bond distances are given in Å.

DFT structures, K^+ interacts with the deprotonated amido nitrogen and the carbonyl oxygen in the secondary coordination sphere. The introduction of K^+ reduced the relative free energy of **Mn-fac** to **Mn-fac_K$^+$** at −15.3 (−12.0) kcal/mol and that of **C-*fac*** from 24.8 (23.2) kcal/mol to **C-*fac*_K$^+$** at 14.1 (17.0) kcal/mol and **TS_*fac*** from 38.7 (27.9) kcal/mol to **TS_*fac*_K$^+$** at 32.9 (25.3) kcal/mol (Figure S11 and Figure 1), such that the overall barrier becomes 48.2 (37.3) kcal/mol in the presence of K^+ counteraction. This barrier is higher than that in the absence of K^+ counteraction, 38.7 (27.9) kcal/mol, as the reactant species is stabilized to a greater extent than the TS species. For the *mer* pathway, the barrier in the presence of K^+, at 27.1 (19.3) kcal/mol, is similar to the barrier in the absence of K^+, at 27.4 (18.5) kcal/mol (Figure 1). Inclusion of one explicit THF molecule coordinated to K^+ gives similar overall barriers of 47.0 (40.3) and 26.6 (18.2) kcal/mol for the formation of the *fac* and *mer* hydride species, respectively (Figure 1). Since this barrier is almost the same as that without K^+ cation (within 1 kcal/mol), for subsequent pathways, we do not consider the effect of K^+ counteraction.

Nevertheless, interconversion of **1-*mer*** to the thermodynamically more stable **1-*fac*** remains feasible through sequential isomerization steps, with an effective barrier of 27.1 (24.0) kcal/mol (via **TS_*fac***) relative to **1-*mer***, Figure 1. The accessibility of both hydride isomers under catalytic conditions provides a mechanistic basis for their distinct roles in the CO_2 to methanol conversion network, wherein **1-*fac*** promotes CO_2 hydrogenation to formic acid and **1-*mer*** facilitates the subsequent reduction toward methanol in the presence of *N*-formylmorpholine, as detailed below.

CO_2 to Methanol Conversion Mechanism for Complex 1

Hydrogenation of CO_2 to HCOOH: 1-*fac* vs 1-*mer*. We explored both ligand-assisted and ligand-participated mechanisms for CO_2 hydrogenation to HCOOH catalyzed by complexes **1-*fac*** and **1-*mer***, with a focus on the involvement of the N–H functionality of the SNS ligand. Our results indicate that the ligand-assisted pathway mediated by **1-*mer*** exhibits an energetic span (δE) of 31.6 (29.8) kcal/mol (see Section S2 of the Supporting Information), which is higher by 3.3 (1.8) kcal/mol than that of **1-*fac*** (δE = 28.3 (28.0) kcal/mol), suggesting that **1-*fac*** serves as the active hydride species for CO_2 hydrogenation to HCOOH. The computed Gibbs free energy profile for the ligand-assisted pathway mediated by **1-*fac*** is shown in Figure 3.

https://doi.org/10.1021/acscatal.6c03391
ACS Catal. XXXX, XXX, XXX–XXX

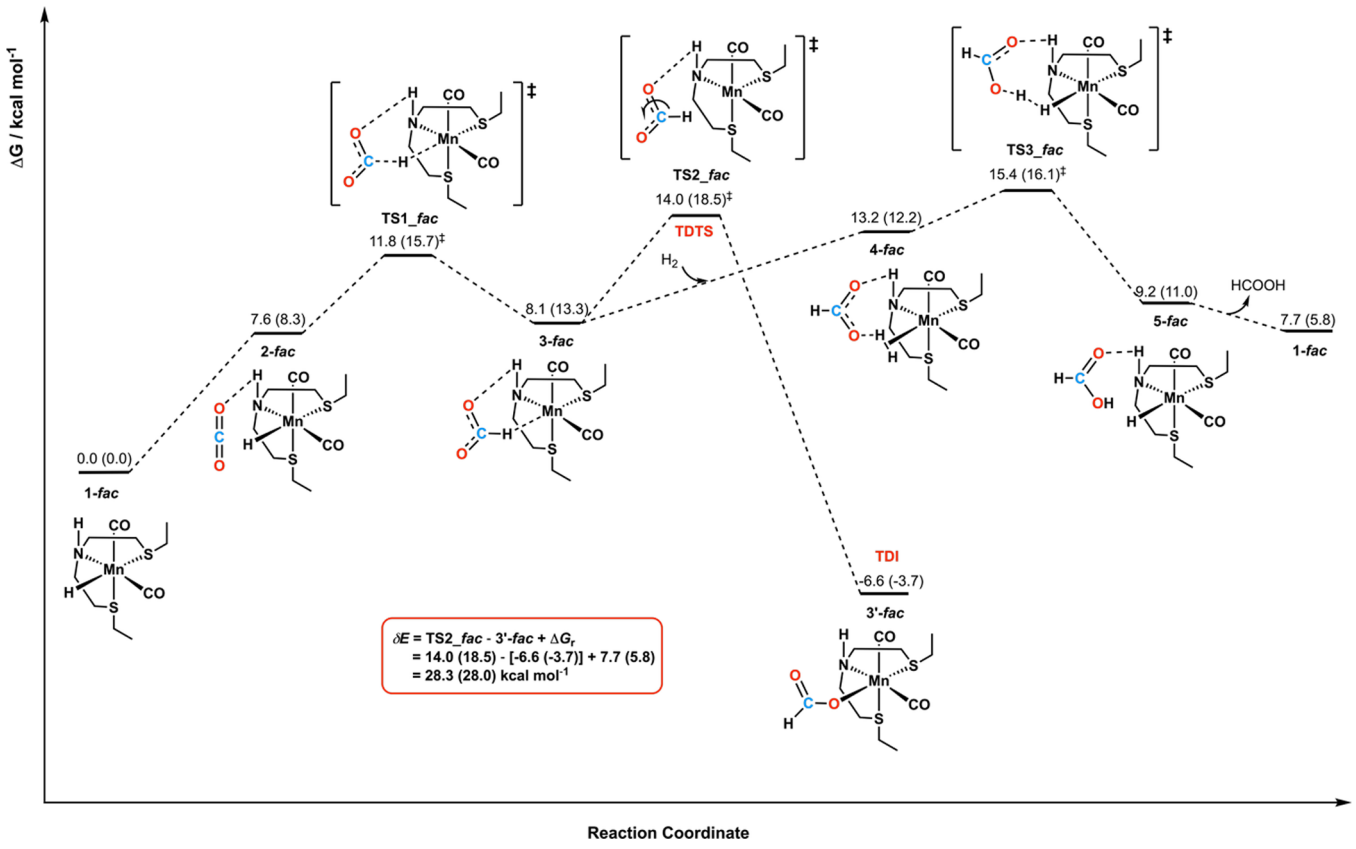

Figure 3. Gibbs free energy profile for CO_2 hydrogenation to HCOOH via the ligand-assisted pathway mediated by **1-*fac***. The free energies were computed at SMD(THF)-B3LYP-D3BJ/def2-QZVP//B3LYP-D3BJ/(def2-TZVPPD for Mn + def2-SVP for all other atoms) level of theory. Corresponding free energies computed at the SMD(THF)-MN15/def2-QZVP//B3LYP-D3BJ/(def2-TZVPPD for Mn, def2-SVP for all other atoms) level are given in parentheses. All values are given in kcal/mol with respect to **1-*fac*** and all other substrates. TDI, turnover frequency-determining intermediate; TDTS, turnover frequency-determining transition state.

While our findings indicate that the ligand-assisted mechanism is the only viable pathway for complex **1-*fac***, the ligand-participated pathway was not operative, as we were unable to locate the key transition state where the N–H functionality facilitates proton transfer to the formate group, a crucial step for the formation of HCOOH, starting from complex **3-*fac***.

Figure 3 presents the free energy profile for the ligand-assisted mechanism of CO_2 hydrogenation to HCOOH. The mechanism begins with the coordination of CO_2 to complex **1-*fac***, forming intermediate **2-*fac***, where CO_2 is hydrogen-bonded to the H atom of the amine group in **1-*fac***, Figure 3. This step is endergonic, with **2-*fac*** lying 7.6 (8.3) kcal/mol above **1-*fac***. From **2-*fac***, the next step involves the hydride transfer from the Mn center to the carbon of CO_2, forming intermediate **3-*fac***, which lies 0.5 (5.0) kcal/mol above **2-*fac***. This step proceeds through **TS1_*fac***, with an activation free energy barrier of 4.2 (7.4) kcal/mol from complex **2-*fac***, Figure 3. Intermediate **3-*fac*** can isomerize to a more stable intermediate **3′-*fac***, lying 14.7 (17.0) kcal/mol below **3-*fac*** and requires overcoming an activation barrier of 5.9 (5.2) kcal/mol via **TS2_*fac***, Figure 4a. Notably, the highly stabilized intermediate **3′-*fac*** is the resting state of the catalytic cycle. Alternatively, intermediate **3-*fac*** can react directly with H_2, forming intermediate **4-*fac***, which lies 5.1 (−1.1) kcal/mol relative to **3-*fac***, Figure 3. From **4-*fac***, heterolytic cleavage of H_2 and the concerted transfer of a proton to the formate moiety yields intermediate **5-*fac***, in which the product HCOOH is hydrogen-bonded to the metal complex via the H atom of the amine group, Figure 3. This step is kinetically facile and proceeds through **TS3_*fac***, with a low activation free energy barrier of 2.2 (3.9) kcal/mol from complex **4-*fac***, Figure 3. Finally, the release of product HCOOH from **5-*fac*** regenerates the starting species **1-*fac***, thus closing the catalytic cycle, Figure 3.

Having established the catalytic cycle, we evaluate the energetic span (δE) by identifying the turnover frequency (TOF) determining intermediate, TDI, and the TOF-determining transition state, TDTS. From Figure 3, it is evident that **3′-*fac*** serves as the TDI, being the most stable intermediate in the cycle, while among the transition states, **TS2_*fac*** is identified as the TDTS as it maximizes δE due to its position prior to the TDI, thereby incorporating the reaction free energy, ΔG_r, Figure 3. The catalytic cycle shows an overall δE of 28.3 (28.0) kcal/mol, indicating that complex **1-*fac*** facilitates the hydrogenation of CO_2 to HCOOH under the experimental reaction conditions (120 °C and 10 atm H_2).

Formylation of Morpholine to *N*-Formylmorpholine

Here, we examine the amidation mechanism of morpholine (**6**) with HCOOH, leading to *N*-formylmorpholine (**14**). A prior DFT study by Mandal et al. has detailed this pathway, which involves the formation of a methylene glycol intermediate, followed by dehydration to yield *N*-formylmorpholine.[32] This

https://doi.org/10.1021/acscatal.6c03391
ACS Catal. XXXX, XXX, XXX–XXX

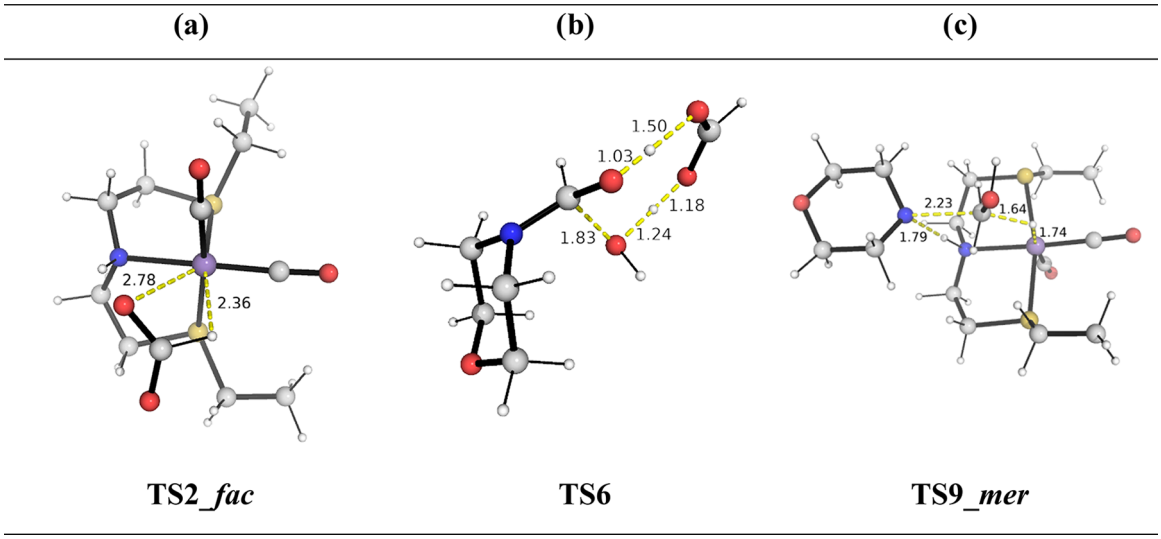

Figure 4. Crucial TS structures for the studied indirect CO_2 hydrogenation to methanol mechanism: (a) isomerization transition state (**TS2_*fac***) in HCOOH formation mediated by **1-*fac***, (b) intramolecular proton transfer transition state (**TS6**) in *N*-formylmorpholine formation, and (c) C–N bond cleavage transition state (**TS9_*mer***) in methanol formation mediated by **1-*mer***. Selected bond distances are given in Å.

metal-free pathway parallels previously reported mechanism[32] and is summarized here with emphasis on the key mechanistic features while noting that differences in the DFT protocol account for variations in the energetics of intermediates and transition states.

The mechanism begins with the interaction of **6** with two molecules of HCOOH in an endergonic process, forming intermediate **7**, which lies 16.3 (16.5) kcal/mol above **6**, Figure 5. Next, intermediate **7** isomerizes to **8** via **TS4**, with an activation free energy barrier of 5.7 (7.7) kcal/mol from **7**. Subsequent proton transfer from the nitrogen atom to the formate moiety in **8** leads to a methylene glycol-based intermediate **9**, where HCOOH is hydrogen-bonded to the nitrogen atom. This step is slightly endergonic, with **9** lying 2.3 (0.2)

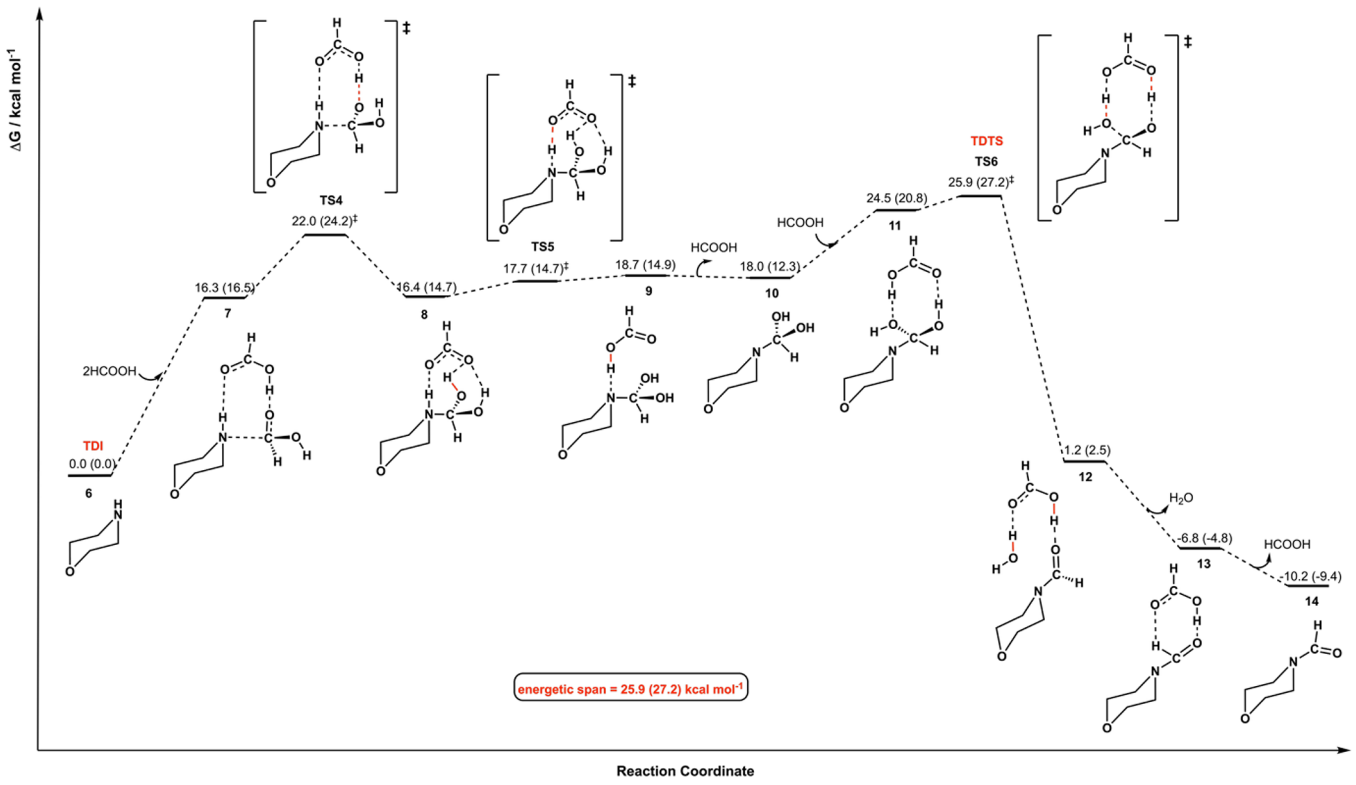

Figure 5. Gibbs free energy profile for the formation of *N*-formylmorpholine. The free energies were computed at the SMD(THF)-B3LYP-D3BJ/def2-QZVP//B3LYP-D3BJ/def2-SVP level of theory. Corresponding free energies computed at the SMD(THF)-MN15/def2-QZVP//B3LYP-D3BJ/def2-SVP level are given in parentheses. All values are given in kcal/mol with respect to the starting complexes, morpholine and HCOOH.

https://doi.org/10.1021/acscatal.6c03391
ACS Catal. XXXX, XXX, XXX–XXX

kcal/mol above **8** and proceeding through **TS5** with a small activation barrier of 1.3 (0.0) kcal/mol, Figure 5. Intermediate **9** then releases HCOOH to form **10**, which reacts with HCOOH to yield intermediate **11**, lying 6.5 (8.5) kcal/mol above **10**, Figure 5. Subsequently, an intramolecular proton transfer between formic acid and the glycol group in **11** leads to the stable intermediate **12**, with the formation of a water molecule. This step is highly exergonic, with **12** lying 23.2 (18.3) kcal/mol downhill of **11** and proceeds via **TS6** (Figure 4b), requiring an activation free energy barrier of 1.4 (6.4) kcal/mol, Figure 5. Finally, in a highly favorable process, intermediate **12** releases H_2O, forming **13**, which then liberates formic acid to yield the final product *N*-formylmorpholine (**14**), Figure 5.

From Figure 5, it is evident that **TS6** represents the TDTS, being the highest energy barrier in the catalytic cycle, while the starting species, morpholine (**6**), is the TDI. The overall δE of 25.9 (27.2) kcal/mol is consistent with the formation of *N*-formylmorpholine under experimental conditions (120 °C and 10 atm H_2).

Hydrogenation of *N*-Formylmorpholine to Methanol: 1-*fac* vs 1-*mer*

In this section, we discuss in detail the hydrogenation of *N*-formylmorpholine (**14**) to methanol catalyzed by complex **1-*fac*** and **1-*mer***, exploring two competing pathways: pathway A (C═O bond hydrogenation followed by C–N bond hydrogenation) and pathway B (C–N bond hydrogenation followed by C═O bond hydrogenation). Our results indicate that pathway A exhibits significantly higher energetic spans for both hydride species, **1-*mer*** (δE = 79.3 (86.7) kcal/mol; Figure 6) and **1-*fac*** (δE = 84.8 (92.1) kcal/mol), indicating that this pathway is unlikely to operate under catalytic conditions (see Section S3 of the Supporting Information for more details). In contrast, pathway B mediated by **1-*mer*** proceeds with an energetic span (δE = 35.0 (32.3) kcal/mol; Figure 7), which is lower by 7.3 (6.3) kcal/mol than that of **1-*fac*** (δE = 42.3 (38.6) kcal/mol; see Section S3 of the Supporting Information), suggesting that **1-*mer*** is the kinetically preferred hydride species for the hydrogenation of *N*-formylmorpholine to methanol.

Pathway A (C═O Hydrogenation Followed by C–N Hydrogenation) Mediated by 1-*mer*. The interaction between complex **1-*mer*** and **14** forms intermediate **15-*mer***, where the carbonyl group of the amide is hydrogen-bonded to **1-*mer***, Figure 6. This step is endergonic, with **15-*mer*** lying 7.8 (11.2) kcal/mol above **1-*mer***. Next, the transfer of hydridic hydrogen atom to the carbon atom of **14** occurs via **TS7_*mer***, with an activation free energy barrier of 10.2 (12.4) kcal/mol from complex **15-*mer***, leading to the formation of intermediate **16-*mer***, Figure 6. Subsequently, proton transfer from the N–H group to the oxygen atom in **16-*mer*** yields intermediate **17-*mer***, wherein the generated hydrogenated *N*-formylmorpholine (**15**) remains coordinated to the Mn and N centers via hydrogen bonds, Figure 6. This step is kinetically facile, proceeding through **TS8_*mer*** with an activation free energy of only 0.2 (−0.5) kcal/mol relative to **16-*mer***. Next, the exergonic release of hydrogenated *N*-formylmorpholine from **17-*mer*** yields the penta-coordinated intermediate **C-*mer***, which lies 10.9 (13.4) kcal/mol below **17-*mer***, Figure 6. From **C-*mer***, coordination of a H_2 molecule at the vacant metal site and its subsequent heterolytic cleavage regenerates the active species **1-*mer***. This step proceeds via **TS_*mer*** with an activation free energy barrier of 27.4 (18.5) kcal/mol from **C-*mer***, Figure 6.

The hydrogenated *N*-formylmorpholine then re-enters the pathway by interacting with **1-*mer*** to form complex **18-*mer***, which lies 8.2 (6.1) kcal/mol above **1-*mer***, Figure 6. Finally, the dissociation of the C–N bond in **18-*mer*** occurs through a

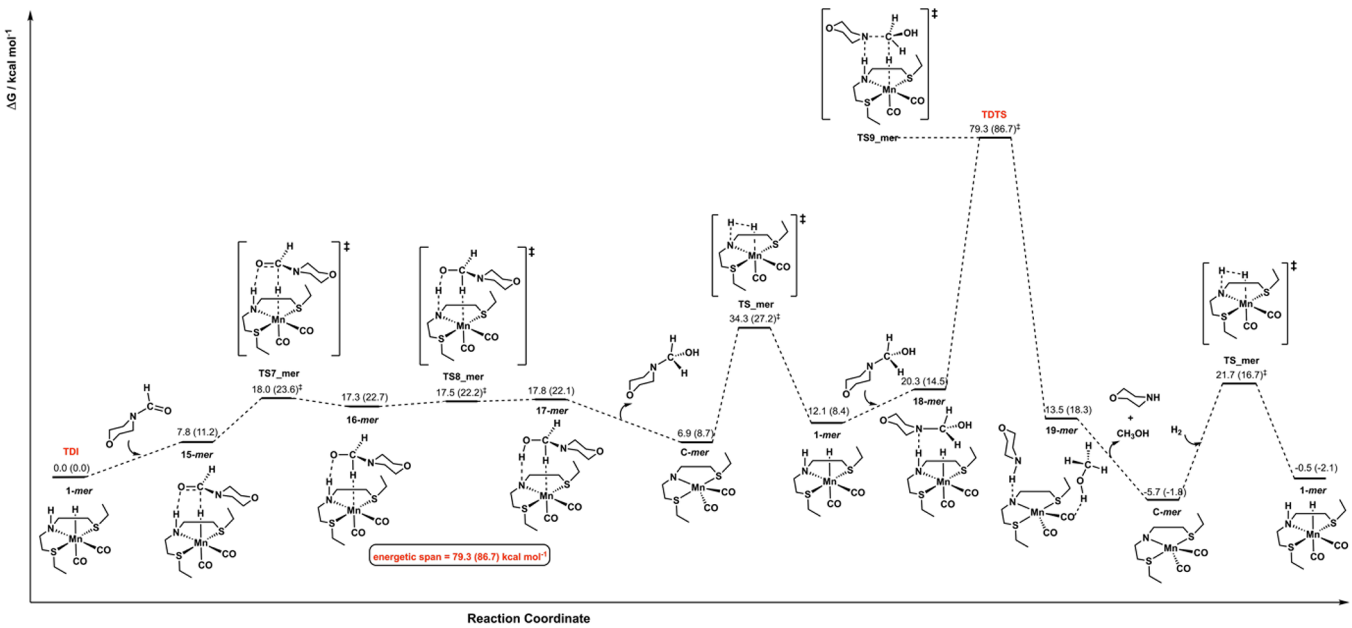

Figure 6. Gibbs free energy profile for *N*-formylmorpholine hydrogenation to methanol via pathway A (C═O bond hydrogenation followed by C–N bond hydrogenation) mediated by complex **1-*mer***. The free energies were computed at SMD(THF)-B3LYP-D3BJ/def2-QZVP//B3LYP-D3BJ/(def2-TZVPPD for Mn + def2-SVP for all other atoms) level of theory. Corresponding free energies computed at the SMD(THF)-MN15/def2-QZVP//B3LYP-D3BJ/(def2-TZVPPD for Mn, def2-SVP for all other atoms) level are given in parentheses. All values are given in kcal/mol with respect to the starting catalyst **1-*mer*** and all other substrates.

https://doi.org/10.1021/acscatal.6c03391
ACS Catal. XXXX, XXX, XXX–XXX

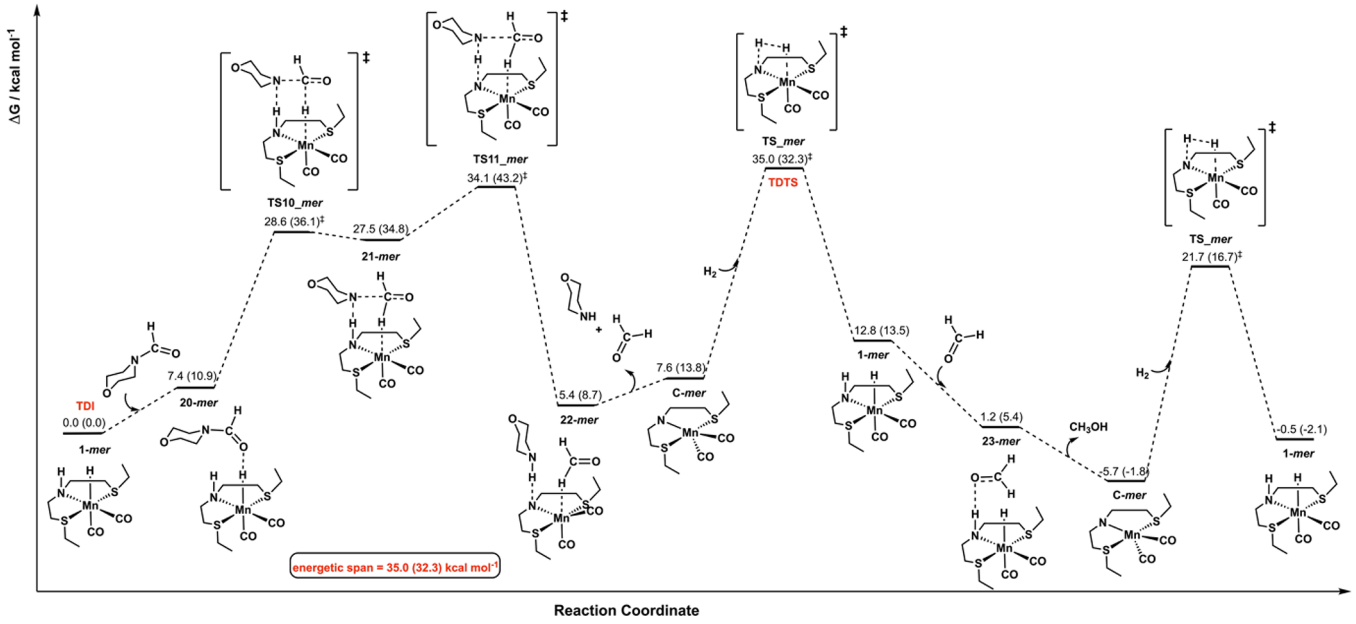

Figure 7. Gibbs free energy profile for *N*-formylmorpholine hydrogenation to methanol via pathway B (C–N bond hydrogenation followed by C═O bond hydrogenation) mediated by complex **1-*mer***. The free energies were computed at the SMD(THF)-B3LYP-D3BJ/def2-QZVP//B3LYP-D3BJ/(def2-TZVPPD for Mn + def2-SVP for all other atoms) level of theory. Corresponding free energies computed at the SMD(THF)-MN15/def2-QZVP//B3LYP-D3BJ/(def2-TZVPPD for Mn, def2-SVP for all other atoms) level are given in parentheses. All values are given in kcal/mol with respect to the starting catalyst **1-*mer***, and all other substrates.

concerted mechanism involving the simultaneous transfer of hydridic and protonic hydrogen atoms to the carbon and nitrogen atoms, respectively, yielding complex **19-*mer***, where the product methanol and regenerated morpholine are weakly coordinated to the metal complex via hydrogen bonds, Figure 6. This step proceeds via **TS9_*mer*** (Figure 4c) with a notably high activation free energy barrier of 59.0 (72.2) kcal/mol, indicating that it is the rate-determining step for the hydrogenation of *N*-formylmorpholine to methanol, Figure 6. Curiously, the DFT study[32] by Mandal et al. did not report this specific step but identified the heterolytic cleavage of H_2 as the rate-determining step for this proposed pathway. Next, an exergonic release of methanol and morpholine from **19-*mer*** regenerates **C-*mer***, which is 19.2 (20.1) kcal/mol lower than **19-*mer***. Subsequent coordination and cleavage of H_2 regenerate the active species **1-*mer***, completing the catalytic cycle, Figure 6. For this studied catalytic cycle, **TS9_*mer*** is identified as the TDTS, while **1-*mer*** serves as the TDI, giving a significantly high δ*E* of 79.3 (86.7) kcal/mol, indicating that the pathway A is unlikely to operate under experimental conditions (120 °C and 10 atm H_2).

Pathway B (C–N Hydrogenation Followed by C═O Hydrogenation) Mediated by 1-*mer*. In an alternative pathway, complex **1-*mer*** coordinates with *N*-formylmorpholine to form complex **20-*mer***, where the oxygen atom of the formyl group is hydrogen-bonded to the metal complex, and lies 7.4 (10.9) kcal/mol above **1-*mer***, Figure 7. Subsequently, the hydride transfer from the Mn center to the carbon atom of the formyl group leads to complex **21-*mer***, characterized by an elongated C–N bond. This transformation is endergonic, with **21-*mer*** lying 20.1 (23.9) kcal/mol above **20-*mer***, and proceeds via **TS10_*mer*** with an activation barrier of 21.2 (25.2) kcal/mol, Figure 7. Next, a concerted dissociation of the C–N bond, accompanied by the transfer of the protonic hydrogen atom from the N–H group to the nitrogen atom of the morpholine moiety, forms complex **22-*mer***, where the resulting morpholine and formaldehyde are hydrogen-bonded to the metal complex, Figure 7. This step proceeds via **TS11_*mer***, with a low activation free energy barrier of 6.6 (8.4) kcal/mol relative to **21-*mer***, Figure 7. The subsequent release of these products yields **C-*mer***, which lies 2.2 (5.1) kcal/mol above **22-*mer***. Following this, heterolytic cleavage of H_2 at the vacant site of **C-*mer*** via **TS_*mer*** regenerates the active species **1-*mer***, with an activation barrier of 27.4 (18.5) kcal/mol, Figure 7. Reintroduction of formaldehyde into the catalytic cycle, accompanied by a concerted transfer of hydridic and protonic hydrogen atoms to the carbon and oxygen atoms of the formaldehyde, respectively, produces complex **23-*mer***, where the desired product methanol is hydrogen-bonded to the metal complex, and lies 11.6 (8.1) kcal/mol below **1-*mer***, Figure 7. Finally, the release of product methanol in an exergonic step regenerates **C-*mer***, which lies 6.9 (7.2) kcal/mol below **23-*mer***, and subsequent H_2 activation at the Mn center in **C-*mer*** regenerates **1-*mer***, thus completing the catalytic cycle, Figure 7.

For this studied catalytic cycle, **TS_*mer*** serves as the TDTS, with **1-*mer*** as the TDI. The δ*E* is calculated to be 35.0 (32.3) kcal/mol, which is significantly lower by 44.3 (54.4) kcal/mol than for the competing pathway A (δ*E* = 79.3 (86.7) kcal/mol). This result suggests that **1-*mer*** catalyzes the hydrogenation of *N*-formylmorpholine to methanol preferably via pathway B, that is, first, C–N hydrogenation, followed by C═O hydrogenation. An inclusion of one explicit THF solvent molecule elevates the barrier of both **TS_*fac*** and **TS_*mer*** due to larger entropic penalty than enthalpic favorability; thus, the inclusion of explicit solvent molecule is not further considered.

The overall energetic span is thus 35.0 (32.3) kcal/mol, with TOF-determining TS as the heterolytic cleavage of H_2 gas (**TS_*mer***). The experimental TON of 60 after 24 h of reaction time

https://doi.org/10.1021/acscatal.6c03391
ACS Catal. XXXX, XXX, XXX–XXX

corresponds to an average TOF of 6.9×10^{-4} s^{-1} and an apparent energetic span of 28.9 kcal/mol at 393.15 K. Accounting for 60 atm H_2, and assuming one H_2 molecule enters between the TDI and TDTS, the calculated span is lowered further by 3.2 kcal/mol. The pressure-corrected MN15 result (δE = 29.1 kcal/mol, 24 h turnover estimate = 47) is therefore close to the experimental value of 60. The lower B3LYP-D3BJ estimate (1.5 turnovers) highlights the exponential sensitivity of predicted rates to modest functional-dependent differences in the calculated energetic span. See detailed analysis in the Supporting Information, Section S10.

Comparison of the barrier height differences for H_2 heterolytic splitting between **TS_*mer*** and ***TS_fac*** (Supporting Information, Section S6), indicates that **TS_*mer*** gives a lower barrier as the H_2 is more polarized (hydridic H has NBO charge of 0.05 a.u., whereas the protic H has NBO charge of 0.30 a.u., Δq = 0.25 a.u) than in **TS_*fac*** (hydridic H has NBO charge of 0.11 a.u. and the protic H has NBO charge of 0.34 a.u., Δq = 0.23 a.u), although the frontier molecular orbitals are similar (Figure 8).

Based on our computational studies, the overall catalytic cycles for Mn-SNS catalyzed CO_2-to-methanol conversion are shown in Scheme 2.

Ligand Environment Effects on Heterolytic H_2 Activation in Mn–SNS Catalysts

Having established the catalytic cycle for CO_2 hydrogenation to methanol mediated by the distinct roles of **1-*fac*** and **1-*mer***, we next examine the rate-determining H_2 cleavage transition state **TS_*mer*** to evaluate how the SNS coordination mode and the nature of the ligand *trans* to H_2 influence this crucial TS barrier, thereby providing insights into tuning the ligand environment in Mn–SNS systems. The calculated activation barrier from **C-*mer*** to **TS_*mer*** is 27.4 (18.5) kcal/mol, which is 13.5 (13.7) kcal/mol higher than the corresponding barrier from **C-*fac*** via **TS_*fac*** (13.9 (4.8) kcal/mol), Figure 1. This difference likely arises from the structural reorganization of **C-*mer*** from a trigonal bipyramidal to a square pyramidal geometry required for H_2 coordination, as well as differences in the electronic nature of the ligand *trans* to H_2 in the *fac* and *mer* coordination mode of the SNS ligand.

To elucidate these effects, we optimized the H_2-coordinated intermediates derived from **C-*fac*** and **C-*mer***. **C-*fac*-H_2** lies at 6.5 (–2.7) kcal/mol relative to **C-*fac*** (Figure 9a), whereas **C-*mer*-H_2** is significantly higher in energy at 20.1 (12.1) kcal/mol relative to **C-*mer*** (Figure 9b). Distortion–interaction analysis indicates that the destabilization of **C-*mer*-H_2** arises from a higher distortion energy (9.4 (10.3) kcal/mol) compared to **C-*fac*-H_2** (4.7 (5.3) kcal/mol), reflecting the energetic penalty associated with rearrangement of the Mn–CO framework (for more details, see Section S4 of the Supporting Information). In addition, the interaction energy in **C-*mer*-H_2** is markedly smaller (–0.2 (–9.1) kcal/mol) than in **C-*fac*-H_2** (–9.8 (–19.7) kcal/mol), consistent with a π-accepting CO ligand *trans* to H_2, which reduces the electron density at the Mn center and weakens H_2 activation.[52] This electronic effect is further supported by the charge distribution and reflected in the structural parameters, Table 1. In **C-*fac*-H_2**, a σ-donating sulfide

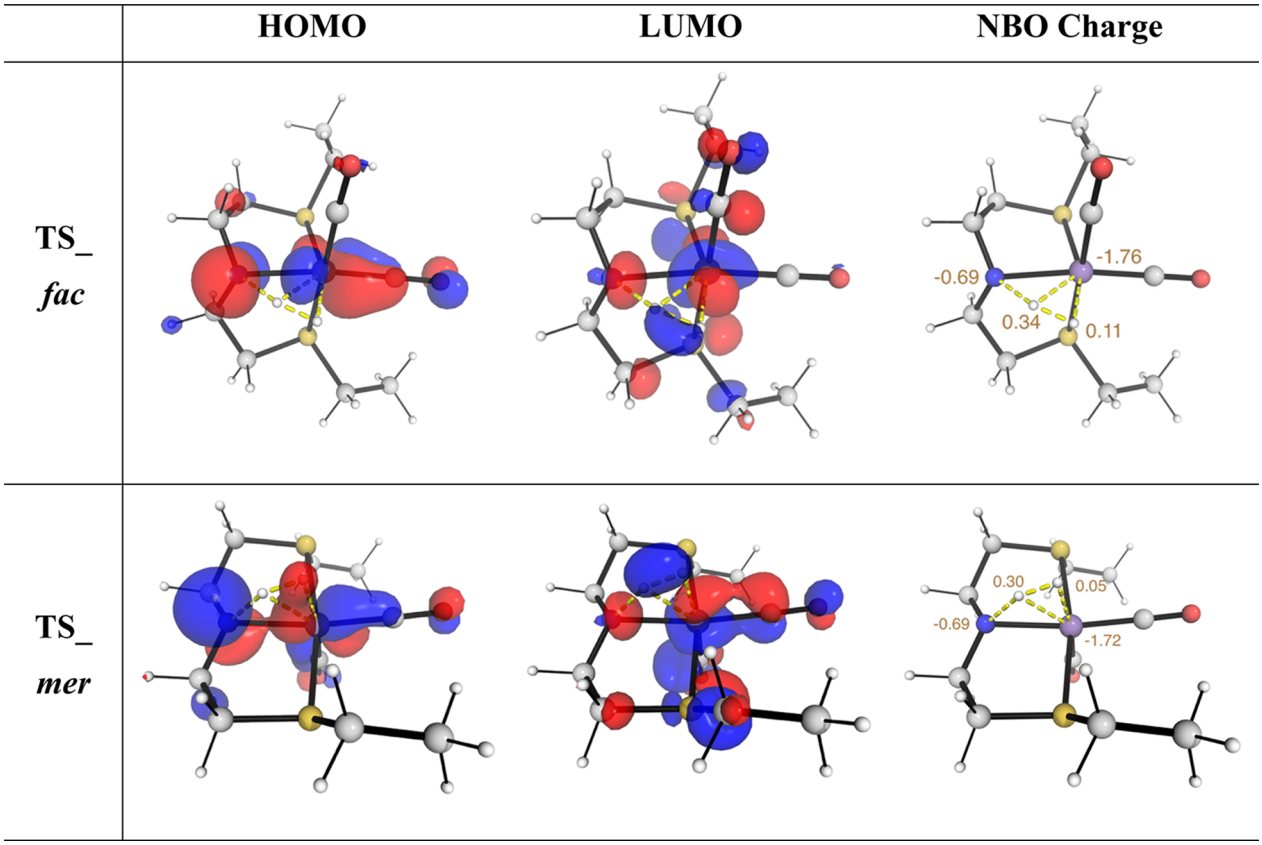

Figure 8. Frontier molecular orbitals (HOMO and LUMO), and natural population analysis (NPA)/natural bond orbital (NBO) charges of **TS_*fac*** and **TS_*mer***.

https://doi.org/10.1021/acscatal.6c03391
ACS Catal. XXXX, XXX, XXX–XXX

Scheme 2. Proposed Catalytic Cycles of Mn-SNS-Catalyzed CO_2-to-Methanol Conversion Based on Our Computational Studies

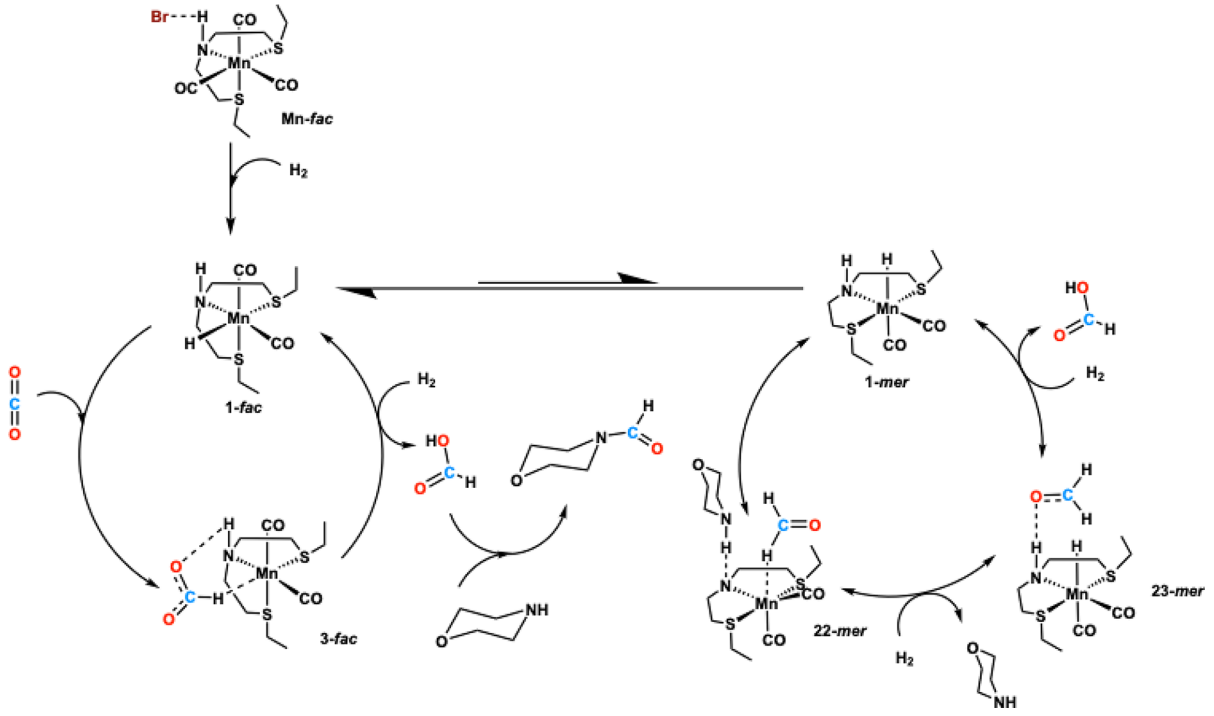

donor occupies the position trans to H_2, increasing the electron density at the Mn center (Δq(Mn) = –0.60), leading to shorter Mn–H distances (1.69–1.71 Å) and a slightly elongated H–H′ bond (0.82 Å), Table 1. In contrast, in **C-*mer*-H$_2$**, the π-accepting CO ligand *trans* to H_2 reduces electron density at the Mn center (Δq(Mn) = –0.32), resulting in longer Mn–H distances (1.83–1.87 Å) and a shorter H–H′ bond (0.79 Å), Table 1. Notably, the N–H′ distance is slightly shorter in **C-*mer*-H$_2$** (2.19 Å) than in **C-*fac*-H$_2$** (2.28 Å), indicating a marginally stronger amido N···H′ interaction in the *mer* configuration, consistent with the more negative charge on nitrogen (Δq(N) = –0.10 vs –0.03).

Interestingly, the heterolytic H_2 cleavage activation barriers from the H_2-coordinated intermediates are nearly identical (**TS_*fac*** = 7.4 (7.5) kcal/mol and **TS_*mer*** = 7.3 (6.4) kcal/mol). Distortion–interaction analysis shows that **TS_*fac*** has higher distortion and more stabilizing interaction energies (13.2 (15.1) and –5.5 (–7.3) kcal/mol), whereas **TS_*mer*** has lower distortion and weaker interaction energies (12.3 (14.4) and –4.8 (–7.8) kcal/mol), resulting in comparable activation barriers. Structurally, **TS_*fac*** exhibits shorter Mn–H distances (1.67 Å) together with an elongated H–H′ bond (0.99 Å), consistent with a more advanced H–H′ bond cleavage, Figure 2a and Table 1. In contrast, **TS_*mer*** shows longer Mn–H distances (~1.75 Å) and a shorter H–H bond (0.96 Å), indicating a less advanced H–H′ activation, Figure 2b and Table 1.

Relative to the H_2-coordinated intermediates, both transition states exhibit similar structural changes. The Mn–H distances decrease marginally (0.01–0.04 Å in **TS_*fac*** and 0.08–0.11 Å in **TS_*mer***), while the H–H′ bond elongates by 0.17 Å and the N–H′ bond shortens by 0.75–0.83 Å, leading to similar N–H′ distances (~1.45 Å). The small Δq(Mn) values (–0.03 for **TS_*fac*** and –0.09 for **TS_*mer***) indicate a minimal additional charge redistribution during the H_2 cleavage step. These features indicate a similar extent of protonic hydrogen (H′)

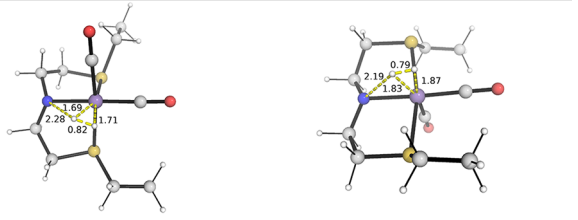

Figure 9. Optimized H_2-coordinated intermediates: (a) **C-*fac*-H$_2$** and (b) **C-*mer*-H$_2$**. Selected bond distances are given in Å.

Table 1. Selected Bond Distances (Å) and Mn Charges (q(Mn) and Δq(Mn)) for the H_2-Coordinated Intermediates (C-*fac*-H$_2$ and C-*mer*-H$_2$) and the Corresponding Heterolytic H_2 Cleavage Transition States (TS_*fac* and TS_*mer*) (The q(Mn) Values for C-*fac* and C-*mer* are –1.13 and –1.32, Respectively)

	C-*fac*-H$_2$	TS_*fac*	C-*mer*-H$_2$	TS_*mer*
Mn–H	1.71	1.67	1.87	1.76
Mn–H′	1.69	1.68	1.83	1.75
H–H′	0.82	0.99	0.79	0.96
N–H′	2.28	1.45	2.19	1.44
q(Mn)	–1.73	–1.76	–1.64	–1.72
Δq(Mn)	–0.60	–0.03	–0.32	–0.09

https://doi.org/10.1021/acscatal.6c03391
ACS Catal. XXXX, XXX, XXX–XXX

transfer in both transition states, consistent with the nearly identical activation barriers.

Taken together, these results indicate that the difference in the overall H_2 cleavage barriers between the *fac* and *mer* pathways ($\Delta\Delta G^{\ddagger} \approx 13.5$ (13.7) kcal/mol) originates primarily from the relative stability of the H_2-coordinated intermediates, governed by ligand rearrangements and the nature of the ligand *trans* to H_2, both dictated by the π-acceptor strength of the ligand. Notably, the related Mn–PNP system, where the PNP ligand adopts a *mer* coordination mode placing a CO ligand *trans* to H_2, shows a comparable heterolytic H_2 cleavage barrier (**TS_*mer*-PNP** = 27.1 (18.7) kcal/mol) to **TS_*mer***, when recalculated using the DFT protocol employed in this study (see Section S5 of the Supporting Information).

To probe the influence of the ligand *trans* to H_2 molecule, we examined model systems in which the CO ligand *trans* to H_2 in **C-*mer*-H$_2$** was replaced with ligands of varying π-acceptor strengths (H_2O, PH_3, and PF_3) and evaluated both the stability of the resulting H_2-coordinated intermediates and the corresponding heterolytic H_2 cleavage barriers. Consistent with the above results, the stability of the H_2-coordinated intermediates follows the π-acceptor strength of the ligand: **C-*mer*-H$_2$_H$_2$O** (10.3 (2.1) kcal/mol) < **C-*mer*-H$_2$_PH$_3$** (17.5 (9.7) kcal/mol) < **C-*mer*-H$_2$** (20.1 (12.1) kcal/mol) < **C-*mer*-H$_2$_PF$_3$** (22.3 (15.8) kcal/mol), which correlates with the corresponding H_2 cleavage barriers: **TS_*mer*_H$_2$O** (18.4 (10.4) kcal/mol) < **TS_*mer*_PH$_3$** (23.7 (16.3) kcal/mol) < **TS_*mer*** (27.4 (18.5) kcal/mol) ≈ **TS_*mer*_PF$_3$** (26.9 (20.9) kcal/mol) (for detailed structural and charge analysis see Section S5 of the Supporting Information). These results further demonstrate that increasing π-acceptor strength of the ligand *trans* to H_2 destabilizes the H_2-coordinated intermediates and consequently leads to higher barriers for heterolytic H_2 cleavage.

CONCLUSIONS

We have performed a comprehensive DFT study on the indirect hydrogenation of CO_2 to methanol catalyzed by a Mn–SNS complex (**Mn-*fac***) in the presence of morpholine as a co-catalyst. The catalytic cycle is initiated by the formation of the active hydride species [MnH–NH] (**1**), where **1-*mer*** is kinetically preferred over **1-*fac*** by 4.9 (5.2) kcal/mol via a facile *fac*-to-*mer* rearrangement. The **1-*mer*** subsequently interconverts to the thermodynamically more stable **1-*fac*** through accessible isomerization steps with an effective barrier of 27.1 (24.0) kcal/mol, enabling the presence of both hydride isomers under catalytic conditions.

Mechanistically, the two hydride isomers **1-*fac*** and **1-*mer***, which can undergo facile *fac*/*mer* isomerization, play distinct roles at different parts of the catalytic cycle. The **1-*fac*** species preferentially catalyzes CO_2 hydrogenation to formic acid, as reflected by a lower energetic span (δE = 28.3 (28.0) kcal/mol) relative to the **1-*mer*** pathway (δE = 31.6 (29.8) kcal/mol). Subsequently, **1-*mer*** promotes the hydrogenation of *N*-formylmorpholine to methanol via a kinetically favorable pathway involving C–N bond hydrogenation followed by C═O bond hydrogenation. This pathway exhibits a lower energetic span (δE = 35.0 (32.3) kcal/mol) than the corresponding **1-*fac*** pathway (δE = 42.3 (38.6) kcal/mol). These findings establish a cooperative catalytic scenario in which **1-*fac*** and **1-*mer*** operate sequentially within the same reaction network. Analysis of the rate-determining heterolytic H_2 cleavage step reveals that the overall activation barrier is primarily governed by the stability of the H_2-coordinated intermediates, which is strongly influenced by the π-acceptor strength of the ligand *trans* to H_2. Model systems incorporating ligands of varying π-acceptor strength (H_2O, PH_3, and PF_3) show that increasing π-acceptor character correlates with higher activation barriers, highlighting the critical role of *trans* ligand in controlling H_2 activation.

Taken together, these results reveal that the Mn–SNS catalyst does not operate through a single static active species, but instead through a dynamic ensemble of *fac*/*mer* hydride isomers that perform complementary catalytic functions. This *fac*/*mer* cooperativity provides a mechanistic basis for understanding how coordination geometry can regulate both the sequence and efficiency of CO_2-to-methanol hydrogenation. More broadly, the identification of trans-ligand-controlled H_2 activation establishes a clear design principle for future Mn-based hydrogenation catalysts: tuning the donor/acceptor properties and spatial arrangement of ligands trans to the H_2 binding site can directly modulate the stability of H_2-coordinated intermediates and, consequently, the overall catalytic barrier. These insights not only rationalize the reactivity of the present Mn–SNS system but also provide a transferable framework for the rational development of more efficient earth-abundant metal catalysts for CO_2 utilization and amine-assisted methanol synthesis.

ASSOCIATED CONTENT

Data Availability Statement

DFT-optimized structures from this study in .xyz format have been uploaded to and are freely available at https://zenodo.org/records/21414490 (DOI: 10.5281/zenodo.21414490). Automation toolkit codes for quantum chemical calculations as well as for thermochemistry analysis and figure plotting are freely available at https://github.com/xinglong-zhang/chemsmart.

Supporting Information

The Supporting Information is available free of charge at https://pubs.acs.org/doi/10.1021/acscatal.6c03391.

Thermodynamic stability of the **Mn-*fac*** and **Mn-*mer*** precatalyst isomers; additional Gibbs free-energy profiles for CO_2 hydrogenation to HCOOH and *N*-formylmorpholine hydrogenation to methanol; distortion–interaction analysis of H_2-coordinated intermediates; ligand-environment and electronic-structure analyses of H_2 coordination and heterolytic cleavage; effects of implicit and explicit THF solvation; effects of the K^+ countercation; energetic-span and turnover-frequency analyses; and absolute electronic energies, zero-point energies, enthalpies, and quasi-harmonic Gibbs free energies for optimized structures (PDF)

AUTHOR INFORMATION

Corresponding Author

Xinglong Zhang – *Department of Chemistry, The Chinese University of Hong Kong, Shatin, New Territories 999077, Hong Kong, China;* orcid.org/0000-0003-1698-692X; Email: xinglong.zhang@cuhk.edu.hk

Authors

Sai V. C. Vummaleti – *Department of Chemistry, The Chinese University of Hong Kong, Shatin, New Territories 999077, Hong Kong, China; Institute of High Performance and*

*Computing (IHPC), Agency for Science, Technology and Research (A*STAR), Fusionopolis Way, #16-16 Connexis, Singapore 138632, Republic of Singapore*

Huiwen Tan – *Department of Chemistry, The Chinese University of Hong Kong, Shatin, New Territories 999077, Hong Kong, China*; orcid.org/0009-0003-9663-7689

Jingyi Liu – *Department of Chemistry, The Chinese University of Hong Kong, Shatin, New Territories 999077, Hong Kong, China*; orcid.org/0009-0007-2296-7668

Complete contact information is available at: https://pubs.acs.org/doi/10.1021/acscatal.6c03391

Author Contributions

[§]S.V.C.V. and H.T. contributed equally. X.Z. obtained funding and conceptualized the project. X.Z. designed the computational studies. S.V.C.V., H.T., and J.L. performed the computational studies under the supervision of X.Z. S.V.C.V., H.T., and X.Z. analyzed the results and wrote the manuscript. All authors contributed to the discussion of the results and approved the final manuscript.

Notes

The authors declare no competing financial interest.

■ ACKNOWLEDGMENTS

The authors acknowledge the use of the computing resources at the Central Research Computing Cluster at the Chinese University of Hong Kong (CUHK), partially funded by the Academic Equipment Fund (Project Number 3036253), for computations performed in this work.

■ REFERENCES

(1) Figueroa, J. D.; Fout, T.; Plasynski, S.; McIlvried, H.; Srivastava, R. D. Advances in CO_2 Capture Technology—The U.S Department of Energy's Carbon Sequestration Program. *Int. J. Greenhouse Gas Control* **2008**, *2*, 9–20.

(2) MacDowell, N.; Florin, N.; Buchard, A.; Hallett, J.; Galindo, A.; Jackson, G.; Adjiman, C. S.; Williams, C. K.; Shah, N.; Fennell, P. An Overview of CO_2 Capture Technologies. *Energy Environ. Sci.* **2010**, *3*, 1645–1669.

(3) Goeppert, A.; Czaun, M.; Prakash, G. K. S.; Olah, G. A. Air as the Renewable Carbon Source of the Future: An Overview of CO_2 Capture from the Atmosphere. *Energy Environ. Sci.* **2012**, *5*, 7833–7853.

(4) Orr Jr., F. M. Carbon Capture, Utilization, and Storage: An Update. *SPE J.* **2018**, *23*, 2444–2455.

(5) Nocito, F.; Dibenedetto, A. Atmospheric CO_2 Mitigation Technologies: Carbon Capture, Utilization and Storage. *Curr. Opin. Green Sustainable Chem.* **2020**, *21*, 34–43.

(6) Álvarez, A.; Bansode, A.; Urakawa, A.; Bavykina, A. V.; Wezendonk, T. A.; Makkee, M.; Gascon, J.; Kapteijn, F. Challenges in the Greener Production of Formates/Formic Acid, Methanol, and DME by Heterogeneously Catalyzed CO_2 Hydrogenation Processes. *Chem. Rev.* **2017**, *117*, 9804–9838.

(7) Sen, R.; Goeppert, A.; Prakash, G. K. S. Homogeneous Hydrogenation of CO2 and CO to Methanol: The Renaissance of Low-Temperature Catalysis in the Context of the Methanol Economy. *Angew. Chem., Int. Ed.* **2022**, *61*, No. e202207278.

(8) Zhong, J.; Yang, X.; Wu, Z.; Liang, B.; Huang, Y.; Zhang, T. State of the Art and Perspectives in Heterogeneous Catalysis of CO_2 Hydrogenation to Methanol. *Chem. Soc. Rev.* **2020**, *49*, 1385–1413.

(9) Wang, J.; Li, X.; Yi, G.; Teong, S. P.; Chan, S. P.; Zhang, X.; Zhang, Y. Non-crystalline Zeolitic Imidazolate Frameworks Tethered with Ionic Liquids as Catalysts for CO_2 Conversion into Cyclic Carbonates. *ACS Appl. Mater. Interfaces* **2024**, *16* (8), 10277–10284.

(10) Boruah, A.; Boro, B.; Wang, J.; Paul, R.; Ghosh, R.; Mohapatra, D.; Li, P.-Z.; Zhang, X.; Mondal, J. Influence of Keto-Enol Tautomerism in Regulating CO_2 Photoreduction Activity in Porous Organic Porphyrinic Photopolymer. *ACS Appl. Mater. Interfaces* **2025**, *17* (1), 1259–1272.

(11) Wang, J.; Li, X.; Teong, S. P.; Chan, S. P.; Li, Z.; Zhang, X.; Zhang, Y. Growth of Ionic Polymers on ZIFs to Construct Core-shell Hybrid Materials via Coordination Interactions for Catalytic CO_2 Conversion. *J. CO2 Util.* **2026**, *104*, No. 103325.

(12) Das, N.; Biswas, C.; Vummaleti, S. V. C.; Azizivahed, T.; Huang, Y.; Wang, W.; Zhang, X.; Mondal, J. Locking of CO_2 in a Bio-inspired Porous-Organic-Polymeric Prison: Impact of Aliphatic Odd-Even Linker Combination. *ACS Mater. Lett.* **2026**, *8* (3), 957–965.

(13) Olah, G. A.; Goeppert, A.; Prakash, G. K. S. *Beyond Oil and Gas: The Methanol Economy*; Wiley-VCH: Weinheim, **2006**.

(14) Goeppert, A.; Czaun, M.; Jones, J. P.; Prakash, G. K. S.; Olah, G. A. Recycling of Carbon Dioxide to Methanol and Derived Products–Closing the Loop. *Chem. Soc. Rev.* **2014**, *43*, 7995–8048.

(15) Olah, G. A.; Goeppert, A.; Prakash, G. K. S. Chemical Recycling of Carbon Dioxide to Methanol and Dimethyl Ether: From Greenhouse Gas to Renewable, Environmentally Carbon Neutral Fuels and Synthetic Hydrocarbons. *J. Org. Chem.* **2009**, *74*, 487–498.

(16) Centi, G.; Perathoner, S. Opportunities and Prospects in the Chemical Recycling of Carbon Dioxide to Fuels. *Catal. Today* **2009**, *148*, 191–205.

(17) Behrens, M.; Studt, F.; Kasatkin, I.; Kühl, S.; Hävecker, M.; Abild-Pedersen, F.; Zander, S.; Girgsdies, F.; Kurr, P.; Kniep, B.; Tovar, M.; Fischer, R. W.; Nørskov, J. K.; Schlögl, R. The Active Site of Methanol Synthesis over $Cu/ZnO/Al_2O_3$ Industrial Catalysts. *Science* **2012**, *336*, 893–897.

(18) Gesmanee, S.; Koo-Amornpattana, W. Catalytic Hydrogenation of CO_2 for Methanol Production in Fixed-Bed Reactor Using Cu–Zn Supported on γ-Al_2O_3. *Energy Procedia* **2017**, *138*, 739–744.

(19) Liu, C.; Yang, B.; Tyo, E. C.; Seifert, S.; DeBartolo, J.; Issendorff, B. V.; Zapol, P.; Vajda, S.; Curtiss, L. A. Carbon Dioxide Hydrogenation to Methanol over Size-Selected Cu_4 Clusters at Low Pressures. *J. Am. Chem. Soc.* **2015**, *137*, 8676–8679.

(20) Graciani, J.; Mudiyanselage, K.; Xu, F.; Baber, A. E.; Evans, J.; Senanayake, S. D.; Stacchiola, D. J.; Liu, P.; Hrbek, J.; Sanz, J. F.; Rodriguez, J. A. Highly Active Copper–Ceria and Copper–Ceria–Titania Catalysts for Methanol Synthesis from CO_2. *Science* **2014**, *345*, 546–550.

(21) Jiang, X.; Nie, X.; Guo, X.; Song, C.; Chen, J. G. Recent Advances in Carbon Dioxide Hydrogenation to Methanol via Heterogeneous Catalysis. *Chem. Rev.* **2020**, *120*, 7984–8034.

(22) Wesselbaum, S.; vom Stein, T.; Klankermayer, J.; Leitner, W. Hydrogenation of Carbon Dioxide to Methanol by Using a Homogeneous Ruthenium–Phosphine Catalyst. *Angew. Chem., Int. Ed.* **2012**, *51*, 7499–7502.

(23) Huff, C. A.; Sanford, M. S. Cascade Catalysis for the Homogeneous Hydrogenation of CO_2 to Methanol. *J. Am. Chem. Soc.* **2011**, *133*, 18122–18125.

(24) Wesselbaum, S.; Mohan, V.; Meuresch, M.; Brosinski, S.; Thenert, K. M.; Kothe, J.; vom Stein, T.; Englert, U.; Hölscher, M.; Klankermayer, J.; Leitner, W. Hydrogenation of Carbon Dioxide to Methanol Using a Homogeneous Ruthenium–Triphos Catalyst: From Mechanistic Investigations to Multiphase Catalysis. *Chem. Sci.* **2015**, *6*, 693–704.

(25) Rezayee, N. M.; Huff, C. A.; Sanford, M. S. Tandem Amine and Ruthenium-Catalyzed Hydrogenation of CO_2 to Methanol. *J. Am. Chem. Soc.* **2015**, *137*, 1028–1031.

(26) Kothandaraman, J.; Goeppert, A.; Czaun, M.; Olah, G. A.; Prakash, G. K. S. Conversion of CO_2 from Air into Methanol Using a Polyamine and a Homogeneous Ruthenium Catalyst. *J. Am. Chem. Soc.* **2016**, *138*, 778–781.

(27) Miller, A. J. M.; Heinekey, D. M.; Mayer, J. M.; Goldberg, K. I. Catalytic Disproportionation of Formic Acid to Generate Methanol. *Angew. Chem., Int. Ed.* **2013**, *52*, 3981–3984.

(28) Savourey, S.; Lefèvre, G.; Berthet, J. C.; Thuéry, P.; Genre, C.; Cantat, T. Efficient Disproportionation of Formic Acid to Methanol Using Molecular Ruthenium Catalysts. *Angew. Chem., Int. Ed.* **2014**, *53*, 10466–10470.
(29) Neary, M. C.; Parkin, G. Dehydrogenation, Disproportionation and Transfer Hydrogenation Reactions of Formic Acid Catalyzed by Molybdenum Hydride Compounds. *Chem. Sci.* **2015**, *6*, 1859–1865.
(30) Schneidewind, J.; Adam, R.; Baumann, W.; Jackstell, R.; Beller, M. Low-Temperature Hydrogenation of Carbon Dioxide to Methanol with a Homogeneous Cobalt Catalyst. *Angew. Chem., Int. Ed.* **2017**, *56*, 1890–1893.
(31) Kar, S.; Goeppert, A.; Kothandaraman, J.; Prakash, G. K. S. Manganese-Catalyzed Sequential Hydrogenation of CO_2 to Methanol via Formamide. *ACS Catal.* **2017**, *7*, 6347–6351.
(32) Mandal, S. C.; Rawat, K. S.; Nandi, S.; Pathak, B. Theoretical Insights into CO_2 Hydrogenation to Methanol by a Mn–PNP Complex. *Catal. Sci. Technol.* **2019**, *9*, 1867–1878.
(33) Grover, J.; Maji, S.; Teja, C.; Al Thabaiti, S. A.; Mostafa, M. M. M.; Lahiri, G. K.; Maiti, D. Base Metal Catalyst for Indirect Hydrogenation of CO_2. *ACS Org. Inorg. Au* **2023**, *3*, 299–304.
(34) Frisch, M. J.; Trucks, G. W.; Schlegel, H. B.; Scuseria, G. E.; Robb, M. A.; Cheeseman, J. R.; Scalmani, G.; Barone, V.; Mennucci, B.; Petersson, G. A.; et al. Gaussian 16, Revision B.01; Gaussian, Inc.: Wallingford, CT, **2016**.
(35) Becke, A. D. Density-Functional Thermochemistry. III The Role of Exact Exchange. *J. Chem. Phys.* **1993**, *98*, 5648–5652.
(36) Lee, C.; Yang, W.; Parr, R. G. Development of the Colle–Salvetti Correlation-Energy Formula into a Functional of the Electron Density. *Phys. Rev. B* **1988**, *37*, 785–789.
(37) Andrae, D.; Häußermann, U.; Dolg, M.; Stoll, H.; Preuß, H. Energy-Adjusted ab Initio Pseudopotentials for the Second and Third Row Transition Elements. *Theor. Chim. Acta* **1990**, *77*, 123–141.
(38) Rappoport, D.; Furche, F. Property-Optimized Gaussian Basis Sets for Molecular Response Calculations. *J. Chem. Phys.* **2010**, *133*, No. 134105.
(39) Weigend, F.; Ahlrichs, R. Balanced Basis Sets of Split Valence, Triple Zeta Valence and Quadruple Zeta Valence Quality for H to Rn: Design and Assessment of Accuracy. *Phys. Chem. Chem. Phys.* **2005**, *7*, 3297–3305.
(40) Weigend, F. Accurate Coulomb-Fitting Basis Sets for H to Rn. *Phys. Chem. Chem. Phys.* **2006**, *8*, 1057–1065.
(41) Grimme, S.; Antony, J.; Ehrlich, S.; Krieg, H. A Consistent and Accurate ab Initio Parametrization of Density Functional Dispersion Correction (DFT-D) for the 94 Elements H–Pu. *J. Chem. Phys.* **2010**, *132*, No. 154104.
(42) Grimme, S.; Ehrlich, S.; Goerigk, L. Effect of the Damping Function in Dispersion Corrected Density Functional Theory. *J. Comput. Chem.* **2011**, *32*, 1456–1465.
(43) Yu, H. S.; He, X.; Li, S. L.; Truhlar, D. G. MN15: A Kohn–Sham Global-Hybrid Exchange–Correlation Density Functional with Broad Accuracy for Multi-Reference and Single-Reference Systems and Noncovalent Interactions. *Chem. Sci.* **2016**, *7* (8), 5032–5051.
(44) Marenich, A. V.; Cramer, C. J.; Truhlar, D. G. Universal Solvation Model Based on Solute Electron Density and on a Continuum Model of the Solvent Defined by the Bulk Dielectric Constant and Atomic Surface Tensions. *J. Phys. Chem. B* **2009**, *113*, 6378–6396.
(45) Grimme, S. Supramolecular Binding Thermodynamics by Dispersion-Corrected Density Functional Theory. *Chem. Eur. J.* **2012**, *18*, 9955–9964.
(46) Schrödinger, LLCThe PyMOL Molecular Graphics System, Version 18; Schrödinger, LLC: New York, NY, **2015**
(47) Zhang, X.; Tan, H.; Liu, J.; Li, Z.; Wang, L.; Chen, B. W. J. CHEMSMART: Chemistry Simulation and Modeling Automation Toolkit for High-Efficiency Computational Chemistry Workflows. *arXiv* **2025**, arXiv:2508.20042.
(48) Kar, S.; Milstein, D. Sustainable Catalysis with Fluxional Acridine-Based PNP Pincer Complexes. *Chem. Commun.* **2022**, *58*, 3731–3746.
(49) Spasyuk, D.; Smith, S.; Gusev, D. G. Replacing Phosphorus with Sulfur for the Efficient Hydrogenation of Esters. *Angew. Chem., Int. Ed.* **2013**, *52*, 2538–2542.
(50) Ye, X.; Plessow, P. N.; Brinks, M. K.; Schelwies, M.; Schaub, T.; Rominger, F.; Paciello, R.; Limbach, M.; Hofmann, P. Alcohol Amination with Ammonia Catalyzed by an Acridine-Based Ruthenium Pincer Complex: A Mechanistic Study. *J. Am. Chem. Soc.* **2014**, *136*, 5923–5929.
(51) Yang, H.; Liu, S.; Dong, H.; Huang, H.; Wang, Y.; Hao, W.; Lan, Y.; Liu, Q. Amplifying the Reactivity of Anionic Mn(I)–H Catalysts via the Cation Effect: Mechanistic Investigation and Application to the Hydrogenation of α-Trisubstituted Carboxylic Esters. *J. Am. Chem. Soc.* **2025**, *147*, 13491–13501.
(52) Kubas, G. J. Hydrogen Activation on Organometallic Complexes and H2 Production, Utilization, and Storage for Future Energy. *J. Organomet. Chem.* **2009**, *694*, 2648–2653.

https://doi.org/10.1021/acscatal.6c03391
ACS Catal. XXXX, XXX, XXX–XXX